Materials Advances

ROYAL SOCIETY OF CHEMISTRY

PAPER

View Article Online
View Journal | View Issue

Cite this: *Mater. Adv.*, 2025, **6**, 7866

Material characterization of NMC black mass from end-of-life lithium-ion batteries for enhanced recycling strategies

Hammad Farooq and Sulalit Bandyopadhyay *

Recycling black mass (BM) obtained from NMC-based end-of-life lithium-ion batteries (LIBs) is intricate and multifaceted due to the complex physicochemical properties of BM and the presence of impurities such as metallic current collectors (Al and Cu), the PVDF (polyvinylidene fluoride) binder, and residual electrolytes. A judicious combination of characterization techniques is essential for understanding the physicochemical properties of BM. This understanding is also vital for optimizing pre-treatment processes designed to remove impurities in BM and for creating a decision framework to efficiently plan subsequent recycling processes. Here, industrial BM samples from end-of-life NMC622, NMC111, and NMC901 LIBs are characterized. Focused beam reflectance measurement (FBRM) was used to develop a method to estimate BM particle size by applying square weighting to chord length distribution, enabling real-time size monitoring during recycling processes. Quantitative phase analysis of XRD patterns was conducted to calculate the fraction (wt%) of crystalline and amorphous phases in BM. Electron microscopy was used to visualize the particle morphology and the deposition of PVDF, while inert thermogravimetry with mass spectrometry (TGA/MS) helped with the identification of carbonaceous and fluorinated gases that evolved during PVDF decomposition. A key contribution of this study was the development of a novel method using oxidative TGA/MS for the quantification of graphite in BM. Additionally, graphite particles were also characterized using Raman spectroscopy, providing insights into the carbonaceous deposits and structural order. Explored characterization techniques highlight the impact of the physicochemical properties of BM and provide a decision framework for selecting pre-treatment methods and optimizing recycling strategies.

Received 26th May 2025,
Accepted 5th September 2025

DOI: 10.1039/d5ma00545k

rsc.li/materials-advances

Introduction

The demand for lithium-ion batteries (LIBs) is projected to increase significantly in the coming years, driven primarily by the increased use of electric vehicles (EV) and renewable energy storage systems. According to a recent study, the demand for LIBs could reach 10 000 GWh by 2040, and meeting this demand just through mining has significant challenges due to limited primary resources.[1] Thus, achieving a sustainable Li supply depends on the presence of well-established recycling procedures for end-of-life LIBs. The market for various LIB chemistries exhibits significant regional variations; in the European Union (EU), NMC chemistry ($Li[Ni_xMn_yCo_z]O_2$) is the most popular choice when it comes to EV and energy storage systems.[2,3] NMC-based LIBs come in several variants defined by their Ni : Mn : Co ratios, *e.g.*, NMC111 ($Li[Ni_{0.33}Mn_{0.33}Co_{0.33}]O_2$) and NMC622 ($Li[Ni_{0.6}Mn_{0.2}Co_{0.2}]O_2$). It is estimated that, by 2050, producing NMC-based LIBs from primary resources will lead to the emission of greenhouse gases totaling 8.2 $GtCO_2eq$,[4] underscoring the environmental benefit of recycling. Black mass (BM), a powder produced by discharging, shredding, grinding, and milling spent LIBs, serves as the primary feed material for downstream pre-treatment and recycling processes. BM contains valuables such as Li, Ni, Mn, and Co, as well as graphite, and has been recently classified as a critical raw material by the EU.[5] The EU battery regulation, which came into force in 2023, ensures minimum recycling targets for these CRMs to be 80% for Li and 95% for Ni and Co by the end of 2031, thus further necessitating the research and investment into LIB recycling.[6]

Material characterization techniques are essential for developing sustainable and efficient pre-treatment and recycling processes. Pre-treatment of BM is carried out to get rid of impurities such as Al, Cu, residual electrolytes, the polyvinylidene fluoride (PVDF) binder, carbon black, and other organic species.[7] Mechanical pre-treatment methods such as crushing,

Particle Engineering Centre, Department of Chemical Engineering, Norwegian University of Science and Technology, Trondheim, 7034, Norway.
E-mail: hammadf@ntnu.no, sulalit.bandyopadhyay@ntnu.no

classification, milling, and sieving are used to liberate the NMC and graphite particles from the current collector (*i.e.*, Al and Cu), while also reducing the particle size to the desired value.[8,9] Separation of Al before hydrometallurgical recycling processes is crucial as it can lead to a reduction in the quality of recycled valuables. Moreover, a reduction in particle size of pre-treated BM due to mechanical pre-treatment increases the specific surface area of the particles, thereby accelerating the leaching kinetics. Pyrolysis of BM is another pre-treatment process for removing organics and fluorine-containing impurities such as the PVDF binder and residual electrolyte salts like ($LiPF_6$). The presence of PVDF is particularly problematic as its hydrophobic nature renders the active material surfaces inert to aqueous solutions, thereby hindering hydrometallurgical processes such as leaching and froth flotation. Furthermore, $LiPF_6$ can react with water to form toxic and corrosive HF gas.[10,11] Pyrolysis at temperatures of 200–400 °C is used to decompose and vaporize volatile organics (such as electrolytes), whereas pyrolysis at temperatures above 500 °C is performed to completely decompose the PVDF binder.[11] Pre-treated BM is then subjected to hydrometallurgical recycling processes, *e.g.*, leaching and froth flotation.

A combination of characterization techniques can offer critical insights into how the physicochemical properties of BM affect pre-treatment and recycling processes, creating a data-driven framework to design and optimize recycling strategies. The particle size of BM is often measured using the laser diffraction (LD) technique, which is a well-established methodology and has been widely adopted by industries.[2,12–15] However, laser diffraction does not readily enable real-time measurements of size needed to optimize pre-treatment and recycling processes. Therefore, this work explores advanced methods like focused beam reflectance measurement (FBRM). Although not yet a routine technique in recycling industries, FBRM provides further insights by enabling real-time size measurements, and it may be established in the future as a valuable analytical tool.[16] X-ray diffraction (XRD) has been used to qualitatively identify the NMC and graphite crystalline phases in BM but overlapping peaks and structural damage hinder reliable quantitative phase analysis. Qualitative characterization of BM samples using XRD has been reported by several studies, where the main findings are focused solely on phase identification and detection of crystalline impurities.[17–21] In this study, XRD patterns of BM samples are refined to perform quantitative phase analysis to obtain critical metrics, such as crystallinity and wt% of different phases in BM. Scanning electron microscopy coupled with energy-dispersive spectroscopy (SEM/EDS) complements XRD by visualizing local morphology and surface chemistry.[22] There are various reports focused on LIB recycling that have employed the SEM/EDS technique to study the particle morphology and surface dispositions within BM samples.[23–26] Other than focusing on particle morphology, this study made significant efforts in determining the wt% of fluorine on the particle surface using EDX analysis. Meanwhile, Raman spectroscopy is used to obtain insights into the structural order of graphite particles by calculating the ratio of D-band intensity to G-band intensity.[18,27–30] A quantitative approach, outlined in this study, requires careful deconvolution and fitting of carbonaceous peaks in the Raman spectra. Thermogravimetric analysis (TGA) coupled with mass spectrometry (MS) is an effective technique for investigating pyrolysis pre-treatment of BM when run under inert conditions, which has been utilized in previous studies to investigate the thermal decomposition profiles of residual electrolytes, organics and the PVDF binder in BM samples.[31–34] In this study, a similar approach is used to perform a comparative analysis of thermal decomposition profiles of residual electrolytes, organics and the PVDF binder among three BM samples. Furthermore, TGA/MS under oxidative conditions has mostly been used to perform ash testing to determine the wt% of total cathode active content in BM samples.[35–39] A quantitative analysis of the TGA/MS results under oxidative conditions is carried out to obtain more helpful information.

In this study, these characterization techniques have been used collectively to assess the physicochemical properties of three different BM samples. The FBRM technique is used to develop a method for the real-time monitoring of the particle size of BM as chord length by comparing the effects of different weighting methods.[40] XRD patterns of three different BM samples are matched with the ICDD (The International Centre for Diffraction Data) database, and the structural parameters are summarized for reference. Quantitative phase analysis of the XRD patterns is performed using Rietveld refinement to determine relative wt% of crystalline phases, as well as using the internal standard method for calculating the amount of amorphous content in BM samples. Particle morphology and surface deposition of the PVDF binder on NMC particles are analyzed using SEM/EDS. Surface deposition of carbonaceous species on graphite particles is analyzed using Raman spectroscopy. A quantitative analysis of TGA/MS under an oxidative atmosphere has been carried out to determine the amount (wt%) of graphite in BM samples. Quantification of graphite in BM is necessary for designing recycling strategies for graphite using processes such as froth flotation. Furthermore, the estimation of the PVDF binder (wt%) using TGA/MS under an oxidative atmosphere is also discussed. TGA/MS under an inert atmosphere is used to analyze the gases that evolved during the decomposition of residual electrolytes, the PVDF binder, and other organic species. These characterization techniques, when used together, can provide a thorough understanding of BM samples, enabling the development of efficient pre-treatment and recycling processes. Furthermore, to demonstrate the practical utility of the developed characterization framework, this study also investigates the physicochemical changes in the BM samples after pyrolysis, a widely used pre-treatment method for the removal of organic species like the PVDF binder.

Materials and methods

Black mass (BM) samples and chemicals

Three distinct BM samples, labeled BM1, BM2, and BM3, were provided by our industrial partner, Hydrovolt. These BM

samples were produced from NMC-based end-of-life LIBs in separate batches; however, since these batches are processed on the same industrial lines, there could be slight cross-contamination between batches. The as-received BM samples had already undergone industrial pre-treatment, which included a low-temperature heat step (<200 °C). The primary purpose of this step was to vaporize volatile organics (such as electrolytes). This temperature is insufficient to decompose the PVDF binder, which therefore remains intact. The BM samples had also undergone mechanical pre-treatment (including shredding, grinding, milling, and sieving) by the industry to reduce the content of Al and Cu foils. The samples provided for this study represent this sieved fraction; however, the specific parameters of the industrial mechanical pre-treatment are unknown. PVDF binder (Sigma-Aldrich 182702), pristine graphite (Sigma-Aldrich 282863), and 1 M $LiPF_6$ in EC/EMC (50/50 v/v; Sigma-Aldrich 746738) were purchased commercially.

Pyrolysis for comparative characterization

Pyrolysis is a widely adopted pre-treatment method for decomposing the PVDF binder and other organics. To illustrate the application of the developed characterization framework, the as-received BM samples were also analyzed after subjecting them to lab-scale pyrolysis. A vertical-style quartz tube furnace was employed for the pyrolysis of BM samples (BM1, BM2, and BM3), where an inert gas (N2) was pumped into the quartz tube from top to bottom. The temperature first increased to 110 °C (held for 3 hours) and then increased to 600 °C at a heating rate of 10 °C min^{-1} and then held there for 1 hour. The pyrolyzed BM1, pyrolyzed BM2, and pyrolyzed BM3 samples were also characterized to determine the phase changes, gas evolution, and surface modifications, thereby providing the critical data needed to guide and optimize recycling processes.

Characterization techniques

PSD was measured using Horiba laser scattering particle size distribution analyzer LA-960 equipped with a wet flow cell where 96% ethanol was used as the dispersion media. For each sample, a specific amount of BM was added to the wet flow cell until a transmittance of 70–80% was reached, at which point the measurement was initiated. For each sample, the reported PSD is measured from a single run. CLD measurements were carried out using the Mettler Toledo ParticleTrack G400 FBRM instrument. For each measurement, a representative mass of the BM sample (1–2 g) was dispersed in 500 mL of 96% ethanol. For each sample, CLD data were acquired continuously for a period of 15 minutes with a sampling interval of 30 seconds. The final reported CLD for each sample represents the time-averaged distribution from these 30 individual measurements.

Digestion of metals in BM samples was carried out using a microwave-assisted digestion instrument called Berghof Speedwave XPERT equipped with DAP-60 digestion vessels. For each measurement, ~100 mg of the BM sample was added to the digestion vessel, followed by the addition of 1 mL of ultrapure water, 7 mL of 37% HCl, and 3 mL of 65% HNO_3 in the same order as mentioned. The temperature was first increased to 180 °C (held for 15 min) and then to 220 °C (held for 30 min). Following digestion, the metal content (wt%) of the solution was measured at three different dilutions using a microwave plasma atomic emission spectrometry (MP-AES) instrument called Agilent MP-AES 4210. The final compositions reported in this study represent the average of these three MPAES measurements, with the associated errors calculated as the standard deviation.

XRD analysis was performed on a Bruker DaVinci1 diffractometer using Cu-Kα radiation (λ = 1.54060 Å), a step size of 0.005°, a time/step of 1 s, a fixed divergence slit (FDS) of 0.2°, and a 2θ range of 15–75°. For XRD analysis, a robust sample preparation procedure was followed, where 9–10 g of each BM sample was first dried in an oven at 60 °C for 24 hours to ensure the removal of moisture and any residual volatile species. Each dried BM sample was then manually ground in a mortar and subsequently sieved using an 80 μm sieve. From this prepared fraction, a single diffraction pattern was collected for each BM sample using a back-loader sample holder to minimize preferred orientation effects. Quantitative phase analysis using Rietveld refinement and the internal standard method was done by employing the fundamental parameters approach (FPA) in the TOPAS software. For the internal standard method, each BM sample was spiked with ~40 wt% of silicon powder (Sigma-Aldrich 215619) as the internal standard.

TGA/MS was carried out on a Netzsch STA 449C Jupiter TGA/DSC coupled with a Netzsch Aëolos QMS 403C. A single analysis was performed for each BM sample under both inert and oxidative conditions to characterize its distinct thermal decomposition profiles. Under inert conditions, ~50 mg of BM in an alumina crucible was heated, where Ar was used as the protective gas (20 mL min^{-1}) and the purge gas (80 mL min^{-1}). The temperature was first increased to 50 °C (held 3 hours) and then ramped to 1000 °C at 5 °C min^{-1} (held 1 hour). For oxidative runs, 20–30 mg of BM was heated under Ar as protective gas (20 mL min^{-1}) and purified air as purge gas (100 mL min^{-1}) to 110 °C (held 1 hour) and then ramped to 1000 °C at 5 °C min^{-1} (held 1 hour). In both cases, the evolved gases from the TGA instruments were directed to the MS using a transfer line heated at 300 °C, which detected species by their m/z ratios (Table S1).

Morphological and elemental analyses of the BM samples were obtained using an SEM Apreo instrument coupled with an EDX Oxford Xmax 80 detector. For each sample, numerous locations across each sample were investigated, and the images and elemental maps presented in this study were selected from this broader investigation as characteristic examples of the distinct cathode and graphite anode particles. High-resolution imaging was performed using an ETD detector at a working distance of ~4 mm, an accelerating voltage of 5–7 kV, and a beam current of ~1.6 nA. For EDX mapping, the working distance was changed to 10 mm, and the current was adjusted to obtain 40–60% detector dead time.

To investigate the structural order of the carbonaceous components, Raman spectroscopy of the BM2 sample was

performed using WITec Alpha 300R instrument equipped with a 532 nm wavelength and a 50x objective (a working distance of 9 mm). To avoid the decomposition of surface carbonaceous species on graphite particles in BM, a low laser power of 0.2–0.5 mW was utilized. To ensure the results were representative of the BM2 sample's heterogeneity, numerous spots on the sample surface were investigated. From this broader investigation, six spectra that captured the range of observed spectral features were selected for detailed deconvolution and fitting, as presented in this study. For deconvoluting and fitting the Raman spectra, the Fityk peak fitting program was used.[41] A linear function was applied to subtract the background, and the 1st-order carbon peaks were fitted using the Lorentzian function, yielding $R^2 > 99\%$. ATR-FTIR (attenuated total reflectance-Fourier transform infrared) spectroscopy of evaporated species from BM3 was performed using the Bruker Vertex 80v instrument in the 500–4000 cm^{-1} wavenumber range at a scan speed of 4 cm^{-1}.

Results and discussion

Particle size, chord length, and metal distribution

Fig. 1a shows the volume-weighted PSDs of BM1, BM2, and BM3 measured by laser diffraction on a logarithmic x-axis, where each sample has a sharp peak at ~15 μm, with mean sizes of ~90 μm (BM1), ~65 μm (BM2), and ~30 μm (BM3). The higher mean sizes for BM1 and BM2 stem from minor peaks at ~200 μm and ~600 μm, indicating a small fraction of large particles. These PSD results from the well-established laser diffraction technique serve as the reference for developing an FBRM-based method to measure chord length distribution (CLD) of the same BM samples (Fig. 1b and c). Laser diffraction works by passing a laser through a dispersed sample and calculating the size from the angular distribution of scattered light.[42] FBRM works by rotating a focused beam in a circular path at a fixed speed and records backward scattered signals only from particles it intercepts.[43] The generated CLD, thus,

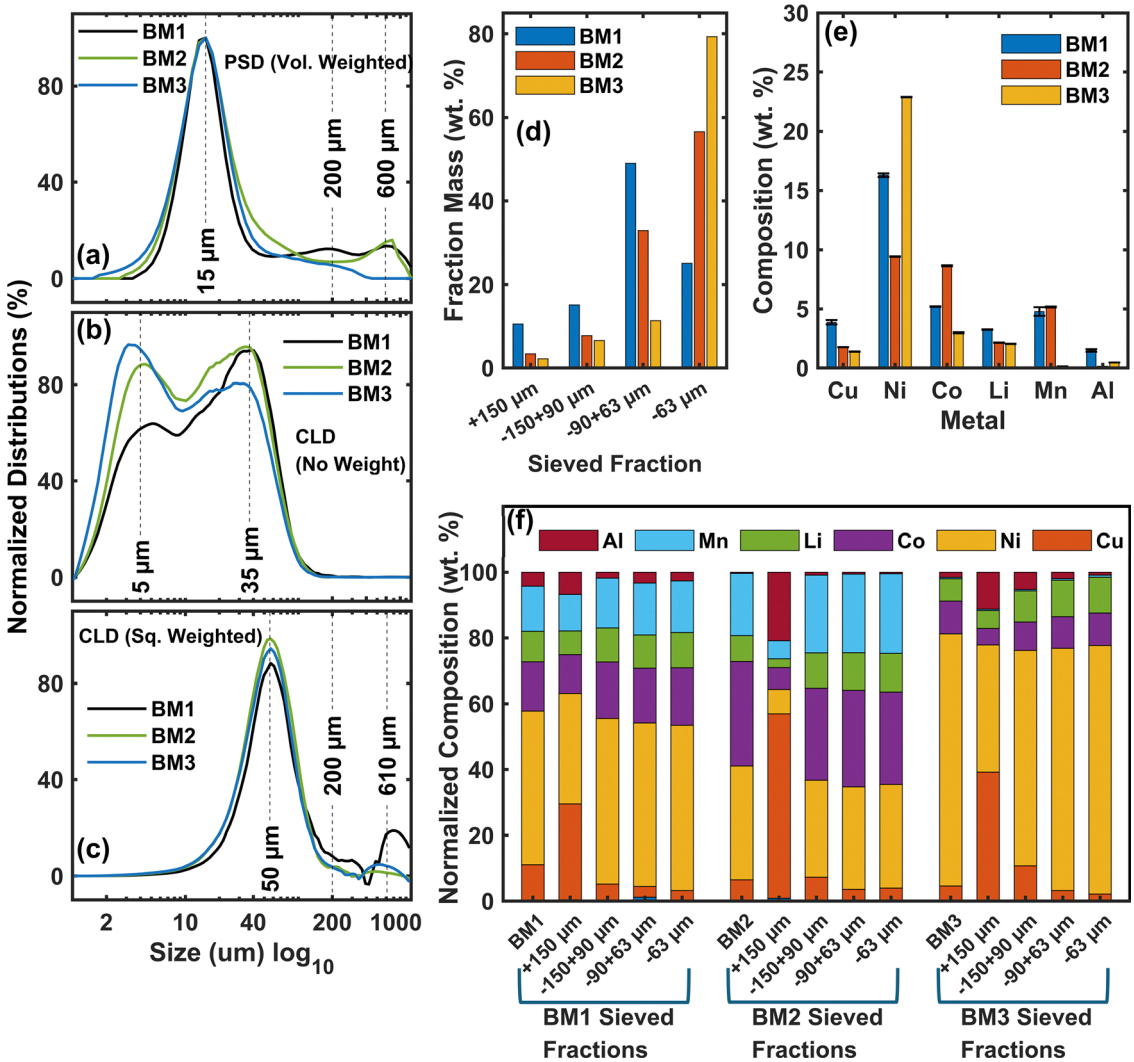

Fig. 1 Particle size, chord length, and metal distributions for BM1, BM2, and BM3 samples: (a) volume-weighted PSD, (b) CLD with no weighting, (c) square weighted CLD, (d) mass distribution (wt%) into four different sieved fractions, (e) metal composition (wt%), and (f) normalized metal composition (wt%) of all four sieved fractions for the three BM samples.

only represents the segments of particles encountered by the beam. CLD measurements are significantly affected by the weighting method applied, particularly in polydisperse samples such as BM. With no weighting, chord length is unbiased but underrepresents larger particles; length weighting enhances sensitivity to elongated particles; square weighting further shifts the mean toward coarser sizes.[40] In this study, the effect of no weighting and square weighting on FBRM results has been analyzed as shown in Fig. 1b and c, respectively, and the results are compared to the PSD measurements in Fig. 1a to identify which weighting best matches the reference distribution.

Fig. 1b (log x-axis) shows that CLD with no weighting has a distinct bi-modal distribution for the three BM samples, where the first peak occurs at ~5 μm and the second peak at ~35 μm. Here, BM1 and BM2 have a mean chord length of ~23 μm and ~20 μm, and BM3 shows a mean chord length of ~15 μm. These findings are noticeably different than those from the PSD measurement in Fig. 1a. Fig. 1c (log x-axis) shows that applying a square weighting to the CLD data lessens the contributions from a smaller size range and enhances the presence of larger particles. Here, a pronounced peak centered at ~50 μm is present for all BM samples, with BM1, BM2, and BM3 exhibiting nearly similar distributions with some variations at higher size ranges. BM1 has a mean size of ~90 μm, BM2 has a mean size of 66 μm, and BM3 has a comparatively lower mean size of ~50 μm (Fig. 1c). The square-weighted CLD results match more closely with the PSD results (Fig. 1a) and exhibit the same trend, *i.e.*, BM3 has a noticeably lower mean size. Square-weighted CLD measurements using FBRM can be used to determine the size of BM particles. This investigation opens significant opportunities for using FBRM as an analytical tool in industrial hydrometallurgical processes.[44] For instance, an FBRM probe could be integrated directly into a leaching process to continuously monitor the changes in the size of NMC particles. Since graphite particles remain inert and do not change size during this process, the real-time data would provide direct insights into the leaching kinetics and subsequent modelling. Similarly, the effect of mechanical pre-treatment of materials on the particle size and slurry properties can also be studied in real-time using FBRM.[44] FBRM has also been employed to optimize collector dosage during the flotation of coal, where a similar mechanism can be employed for the flotation of graphite from BM.[45] Despite its promising industrial applications, the FBRM technique is limited by its measurement of particle chord length instead of actual size, making particle shape and orientation significant influencing factors. As the particle shape deviates from spherical, the FBRM measurements can be significantly affected by the orientation of the particles.[46] FBRM performance can also be hindered in highly concentrated and opaque slurries where laser penetration is limited.[47]

Fig. 1d shows the weight distribution of three BM samples sieved into four different size fractions of +150 μm, −150 + 90 μm, −90 + 63 μm, and −63 μm. Fig. 1d shows that ~80 wt% of BM3 is present in −63 μm fraction, while BM1 and BM2 have only ~55 wt% and ~25 wt% in −63 μm fraction. Additionally, BM1 has a higher mass in the +150 μm (10 wt%), −150 + 90 μm (15 wt%), and −90 + 63 μm (50 wt%) fractions compared to BM2 and BM3. The sieve analysis highlights the heterogeneous nature of the three BM samples in terms of their particle size distributions. The heterogeneous nature of BM materials is a key challenge in recycling, *i.e.*, industrial BM feed is not a uniform material, and its physical properties can differ significantly depending on the source of spent LIBs and processing history.

Beyond physical heterogeneity, the BM samples also exhibit significant chemical heterogeneity, both between the different sample types (Fig. 1e) and within the sieved fractions of a single sample (Fig. 1f). Fig. 1e shows the metal composition (wt%) for the three BM samples, where BM1 contains slightly higher Li (3.25 ± 0.02 wt%) compared to BM2 (2.15 ± 0.01 wt%) and BM3 (2.04 ± 0.02 wt%). The total mass (sum of wt% of all metals) from metal composition results (Fig. 1e) only accounts for ~35 wt% for BM1, ~27 wt% for BM2 and ~30 wt% for BM3. The remainder in each BM is mainly graphite and oxides, as well as relatively small amounts of PVDF binder, electrolytes, and other organic species. Table 1 shows the molar ratio of Ni : Mn : Co for the three BM samples and reveals that BM1, BM2, and BM3 could have been produced from NMC622 ($Li[Ni_{0.6}Mn_{0.2}Co_{0.2}]O_2$), NMC111 ($Li[Ni_{0.33}Mn_{0.33}Co_{0.33}]O_2$), and NMC901 ($Li[Ni_{0.9}Mn_0Co_{0.1}]O_2$ or $Li[Ni_{0.9}Co_{0.1}]O_2$) type end-of-life LIBs, respectively. NMC622 in BM1 is a nickel-rich variant of NMC that has notably higher specific capacity than NMC111 in BM2.[48,49] BM1 is most likely produced from spent LIBs from EVs where demand for longer driving ranges and faster charging speeds is high.[49] NMC111 in BM2 is known for its excellent capacity retention and thermal stability,[50] thus, BM2 is most likely produced from spent EV batteries where battery longevity and thermal stability are desired. Furthermore, BM3 originates from NMC901 type spent LIBs (Table 1), where NMC901 is a relatively new high-nickel layered oxide cathode.[51] NMC901 has seen rising usage in EVs due to its significantly higher energy density and remarkably good reversible capacity.[52] The presence of a very small amount of Mn in the BM3 is likely due to minor cross-contamination during the industrial-scale BM production. Although further confirmation of NMC phases using XRD is needed, the molar ratios of Ni:Mn:Co for each BM (Table 1) suggest that the three BM samples in this study originated from distinct and well-defined NMC chemistries with slight cross-contamination during the industrial BM production process. However, many commercial recycling facilities could process a highly heterogeneous feedstock, often consisting of a mixture of different chemistries of LIBs. Such mixing would result in a BM sample with a more complex and heterogeneous elemental composition. Fig. 1f shows the normalized metal composition (wt%) for BM1, BM2, and BM3, including the sieved fractions of each BM. The results show that the elemental distribution is not uniform across the different size fractions. A critical finding is that metallic impurities (Al and Cu) are primarily concentrated in the larger size fractions (+150 μm and −150 + 90 μm) across all three samples, demonstrating within-sample heterogeneity.

Table 1 Amount (wt%) of Ni, Mn, and Co in the three BM samples along with the molar ratio between Ni : Mn : Co

BM Sample	Ni (wt%)	Mn (wt%)	Co (wt%)	Ni : Mn : Co molar ratio
BM1	16.29	4.78	5.19	6 : 2 : 2
BM2	9.43	5.16	8.64	1 : 1 : 1
BM3	22.90	0.13	2.98	9 : 0 : 1

The distribution of Ni, Mn, and Co remains relatively uniform across all size fractions while maintaining the molar ratio characteristic for each BM (Table 1). The characterization results presented in Fig. 1 are representative of the analyzed fraction. It is important to acknowledge that due to the inherent heterogeneity of these industrial BM samples, a single analysis may not capture the full variability of a big batch. A robust industrial quality control protocol would therefore require a comprehensive sampling plan with multiple analyses from different locations within a batch to fully account for this heterogeneity.

Phase identification and quantitative phase analysis

Fig. 2 shows the quantitative phase analysis (QPA) of XRD patterns of BM1, BM2, and BM3 using both Rietveld refinement (Fig. 2a–c) and the internal standard method (Fig. 2d-f). Pattern matching XRD reflections with the ICDD database reveal that $Li[Ni_xMn_yCo_z]O_2$ (*i.e.*, NMC) and graphite are the two crystalline species detected in all BM samples. Here, graphite in each BM belongs to the 2H (hexagonal) phase with the main characteristic reflection (0 0 2) at ~26.5° (ICDD 00-056-0159). The characteristic reflection for NMC (0 0 3) in all BM samples appears at ~18.6°.[53] Due to identical peak positions for different NMC chemistries, distinguishing between them by just pattern matching is complicated. However, combining the XRD results

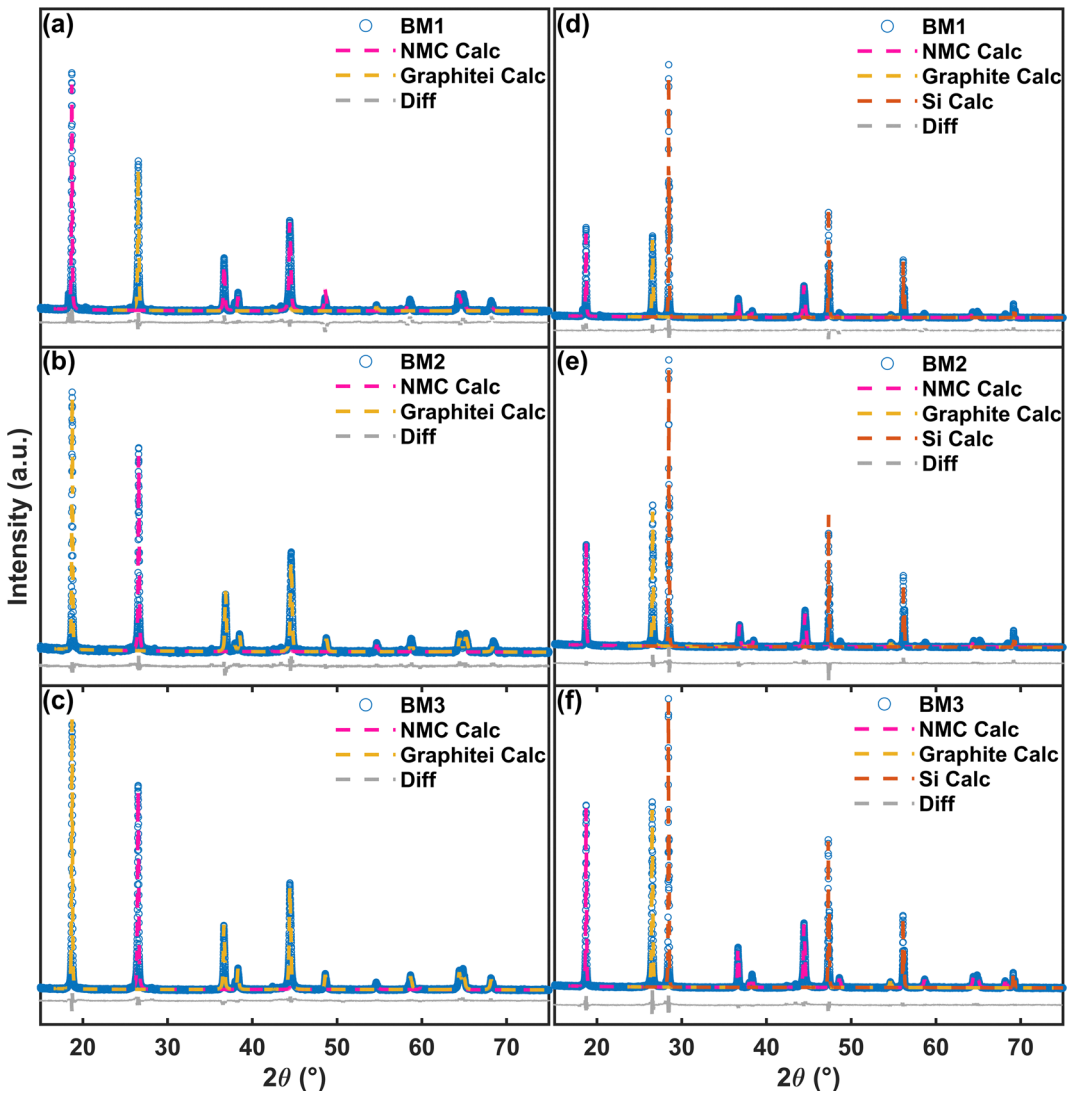

Fig. 2 XRD patterns of BM samples from 2θ of 15° to 75°. (a)–(c) Rietveld refinement of BM1, BM2 and BM3 XRD patterns. Goodness-of-fit (GOF) obtained upon Rietveld refinement of BM1, BM2, and BM3 XRD patterns is 2.22, 1.41, and 1.68, respectively. (d)–(f) Quantitative phase analysis of BM1, BM2, and BM3 XRD patterns using the internal standard method, where Si is used as the internal standard at ~40 wt% spiked amount, and a GOF value of 1.95, 1.59, and 1.78 is obtained for BM1, BM2, and BM3, respectively.

(well-preserved crystalline phases) with metal composition analysis (Table 1) enables the specific identification of BM1 as NMC622 (ICDD 00-066-0854), BM2 as NMC111 (ICDD 00-062-0431), and BM3 as NMC901 (ICDD 00-062-0470). The lattice parameters and structure data for each phase are summarized in Tables S2 and S3. ICDD entries (Table S2) show that the NMC cathode in BM samples exists as a crystalline oxide with an R-3m structure, where transition metals are in higher oxidation states (Ni^{3+} in BM1 and BM3, Ni^{2+} in BM2, Co^{3+}, Mn^{4+}). During acid leaching to recycle these metals, the transition metals must be reduced to their lower oxidation states (Ni^{2+} for BM1 and BM3, Co^{2+}, Mn^{2+}). A complete dissolution of transition metals in acids, thus, requires the use of a reducing agent (such as H_2O_2) or acids like HCl that can generate Cl_2 to oxidize.[54] Lithium, however, is leached out as Li^+ without needing reduction.[54] Graphite, the other crystalline phase detected in BM samples, is chemically inert during acid leaching. However, the presence and amount of graphite must be considered, as it can significantly modify the slurry properties and complicate downstream processing such as filtration.

These findings are further used for the QPA of XRD patterns by both Rietveld refinement and the internal standard method. Fig. 2a–c shows the Rietveld refinement of BM1, BM2, and BM3 XRD patterns, along with the difference between experimental and calculated patterns. The Rietveld refinement indicates that the relative wt% of graphite and NMC varies across the BM samples, where the graphite content is 36.2% for BM1, 41.2% for BM2, and increased to 47.3% for BM3. Correspondingly, the amount of NMC phase is 63.8 wt%, 58.8 wt%, and 52.7 wt% for BM1, BM2, and BM3, respectively. The varying wt% of the NMC cathode in each BM sample is a valuable finding since different NMC types (*e.g.*, NMC622, NMC111, and NMC901) exhibit varying leaching behaviors. Ni-rich cathodes (*i.e.*, NMC901 in BM3) tend to dissolve more readily and require a less reductant, since they contain less Mn.[55] By contrast, cathodes with a higher Mn or Co (*i.e.*, NMC111 in BM2) content may need stronger reducing conditions or longer leaching times to achieve complete extraction of metals.[55] Thus, the measured phase fractions enable adjusting the acid concentration and reductant dosage to match the actual NMC content and chemistry in the feed. Fig. 2d–f shows the refinement of XRD patterns for BM1, BM2, and BM3 using the internal standard method, where Si is spiked as the internal standard. The QPA results from this internal standard method show similar NMC phase amounts to the Rietveld refinement results; 62.1 wt% for BM1, 57.8 wt% for BM2 and 54.7 wt% for BM3. However, the absolute graphite content determined by the internal standard method decreased to 26.1 wt% for BM1, 32.0 wt% for BM2, and 37.2 wt% for BM3. This reduction is attributed to the presence of amorphous species like the PVDF binder, water-soluble binders, possibly amorphous oxidized species and other carbonaceous materials. It is reported that the highly crystalline NMC particles, like the ones in the analyzed BM samples, tend to be more resistant to leaching, as the stable, defect-free structure limits acid access and slows dissolution.[56] In contrast, amorphous phases dissolve more readily than their crystalline counterparts due to their less ordered, more permeable structure.[57]

The internal standard method shows an amorphous content of 11.8 wt%, 10.2 wt%, and 8.1 wt% for BM1, BM2, and BM3, respectively. The PVDF binder is present on the surface of NMC cathode active particles, creating a passivation layer that severely hinders the reaction of leaching reagents to the reactive surfaces. It has been demonstrated that removing this amorphous binder fraction can increase leaching efficiency.[58] Moreover, coating of the PVDF binder renders the cathode particles hydrophobic, making the separation of graphite and the NMC cathode *via* froth flotation less efficient. The most used pre-treatment method to get rid of this PVDF binder is the pyrolysis of BM samples. Fig. S3 presents the XRD patterns of pyrolyzed BM1, pyrolyzed BM2, and pyrolyzed BM3. It has been reported that during pyrolysis, graphite acts as a reducing agent, converting the transition metals in $Li[Ni_xMn_yCo_z]O_2$ partially or fully to their respective oxides (*e.g.*, NiO, MnO) and metallic phases (*e.g.*, Ni, Mn, Co).[32] Simultaneously, this carbothermic reduction of the NMC cathode causes Li in the $Li[Ni_xMn_yCo_z]O_2$ crystalline lattice to transform into highly water-soluble phases (Li_2CO_3 and Li_2O).[32] Consequently, this enables a more sustainable and efficient recycling pathway where Li can be selectively recovered from pyrolyzed BM by simply leaching the pyrolyzed BM with water as the leaching reagent. Subsequently, the Li-depleted pyrolyzed BM can be subjected to further hydrometallurgical processes, such as total acid leaching to first recover transition metals or froth flotation to first recover graphite. Further insights into the pyrolysis pre-treatment of NMC BM can be acquired by analyzing the gases evolved from the reduction reactions as well as from the decomposition of organic species (electrolytes, PVDF, surface coatings).

Identification of gases evolved under pyrolytic conditions

Fig. 3 shows the TGA/MS analysis of BM1, BM2, and BM3 samples carried out under pyrolytic conditions (*i.e.*, argon gas) to study the mass change happening due to different reactions and analyze the gases evolved during the process. Pyrolysis pre-treatment not only results in phase transformations of $Li[Ni_xMn_yCo_z]O_2$ and graphite (as shown by the XRD patterns of pyrolyzed BM in Fig. S3) but also removes organic impurities from particle surfaces (such as electrolytes, PVDF, and other organic species).[31,32]

Fig. 3a–c show that the mass loss occurred in samples BM1, BM2, and BM3, respectively, within the temperature range of 50–200 °C, is ~4–5 wt%. MS spectra of BM1, BM2, and BM3 in Fig. 3d–f, respectively, show that this mass loss is attributable to evaporation of EMC (ethyl methyl carbonate) and decomposition of other electrolyte solvents such as EC (ethylene carbonate). This is in agreement with findings by Tao *et al.*, who reported a 2.42 wt% loss in the 100–200 °C range from electrolyte volatilization and $LiPF_6$ decomposition.[31] Similarly, Huang *et al.* observed an 8.62 wt% loss below 200 °C from the same source.[32] Fig. 3e shows that the BM2 sample also gives rise to various MS signals other than just the EMC MS signal within the 50–200 °C temperature range, such as PO (propylene carbonate), HF, CH_4, and CO. These species likely originate

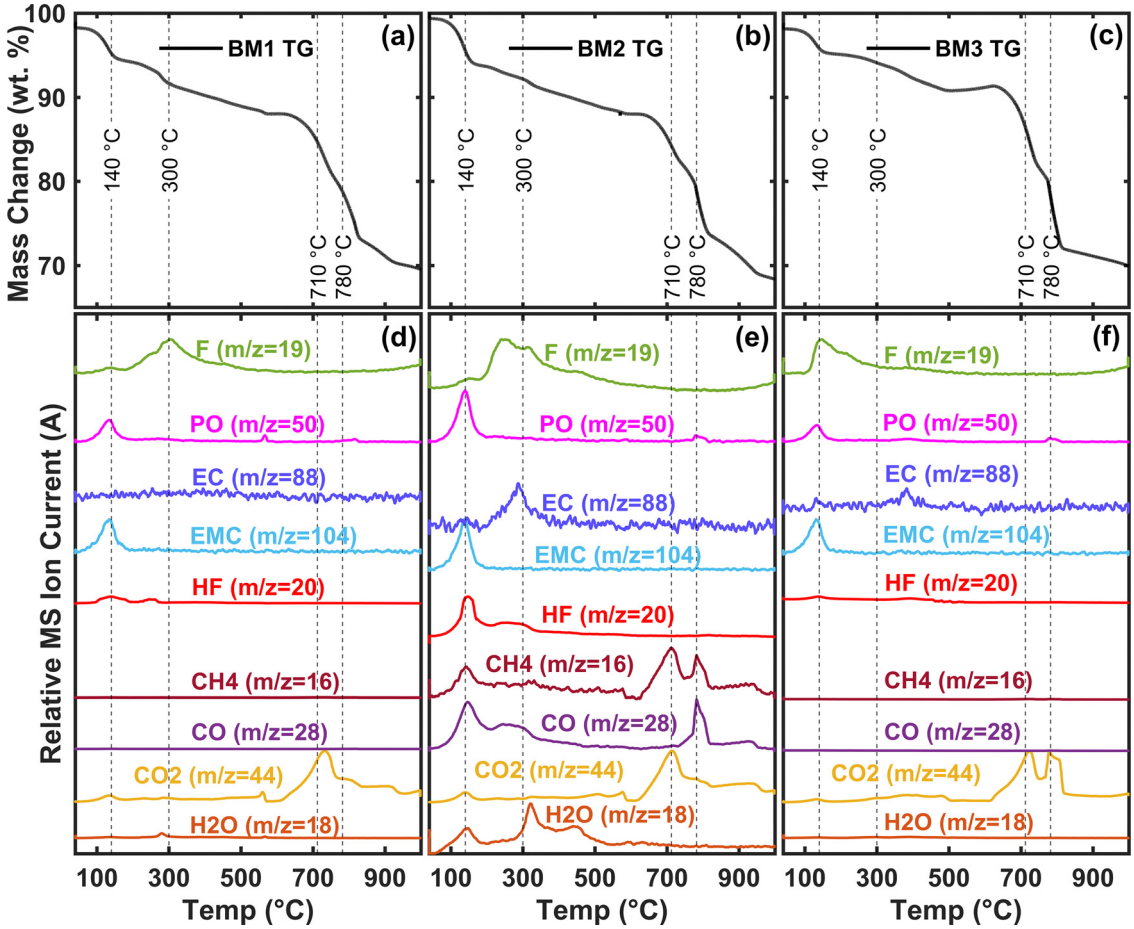

Fig. 3 TGA/MS measurements of the three BM samples carried out in an inert atmosphere to examine the evolved gases. (a) TGA mass loss for BM1, (b) TGA mass loss for BM2, (c) TGA mass loss for BM3, (d) relative MS spectra of evolved species shown as ion current (in A) for BM1, (e) relative MS spectra of evolved species shown as ion current (in A) for BM2 and (f) relative MS spectra of evolved species shown as ion current (in A) for BM3.

from the decomposition of other carbonate-based electrolyte solvents, while the detection of HF suggests the decomposition of the $LiPF_6$ in BM2.[31] The results indicate that despite undergoing low-temperature treatment (<200 °C), these BM samples retain residual electrolytes. This can be explained by the strong physical adsorption of electrolyte solvents onto the surface and into the pores of active material particles, a mechanism that hinders their complete removal at low temperatures.[31,32] TGA/MS analysis of pure 1.0 M $LiPF_6$ in EC/EMC under inert conditions (Fig. S4a and b) further supports these findings. Moreover, the ATR-FTIR spectrum of evaporated species captured from BM2 and BM3 at 200 °C (Fig. S4c) partially matches the ATR-FTIR spectrum of pure $LiPF_6$ in the EC/EMC reference sample, confirming that the evaporated species within the 50–200 °C range are residual electrolytes. It should be noted that the peaks corresponding to $LiPF_6$ are not detected in the ATR-FTIR spectra of evaporated species captured from BM2 and BM3 since $LiPF_6$ would have decomposed during the evaporation and capturing process. This is also shown in Fig. 3e where the variety of evolved gases in the BM2 sample, including HF and CO, is consistent with the decomposition of $LiPF_6$ and carbonate solvents.[33]

Fig. 3a-c shows a mass loss of ~4 wt% within the 200–500 °C temperature range for the three BM samples and can be attributed mainly to the decomposition of the PVDF binder. The decomposition temperature of the PVDF binder is reported to be ~475 °C.[19] However, it can start to decompose at ~380 °C, and the majority of PVDF decomposes by ~500 °C, as shown by TGA/MS analysis of pure PVDF in Fig. S5a and b. It is also important to note that PVDF can form a liquid film around 400–500 °C, coating the active particles. This phenomenon, described by Huang *et al.*, can trap organic residues and influence the uniformity of gas evolution and reduction reactions, potentially explaining the minor variations observed between BM1, BM2, and BM3 samples.[32] This can hinder the complete removal of organic substances and cause reactions between fluorinated gases and metal oxides, leading to the formation of metal fluorides that remain as contaminants.[32] During this stage, hydrogen (H_2) and various small-molecule hydrocarbons have been reported to be produced in previous studies from the thermal degradation of separator materials.[31] These gases are not detected in the inert TGA/MS of BM1, BM2, and BM3 since these samples do not contain polymeric separator materials. Previous studies have reported the formation of

HF gas during the decomposition of the PVDF binder. In this study, mainly the fluorine gas is detected along with carbonaceous gases like CO_2.[31]

As the temperature reaches 500 °C, $Li[Ni_xMn_yCo_z]O_2$ cathode particles react with graphite under an inert atmosphere and reduce into separate metal oxides (NiO, CoO, and MnO), as shown in eqn (S1) and (S2). This is characteristic of the carbothermic reduction of the NMC cathode material. Further increase in temperature (Fig. 3) results in a significant mass loss of ~20 wt% within the 500–800 °C region for BM1, BM2, and BM3. This is caused by the further reduction of metal oxides (such as NiO, MnO and CoO) into metallic phases (such as Ni, Co). This finding is strongly supported by Tao *et al.*, who identified a major weight loss stage (7.70 wt%) between 650 °C and 800 °C, corresponding to the reduction of NiO and CoO to their metallic states, accompanied by the evolution of CO_2, CO, and CH_4.[31] These findings are in agreement with the XRD analysis of pyrolyzed BM (Fig. S3). MS spectra of each BM1, BM2, and BM3 in Fig. 3d, e, and f, respectively, show that mass loss within this region produces a large amount of CO_2 gas, whereas BM2 also produces MS spectra for CO as well as CH_4 gases within this region.

Quantification of graphite using TGA/MS

TGA/MS running in an oxidative atmosphere is used in this study to develop a reliable method for approximate quantification of total carbon in BM samples. When NMC BM is heated under excess O_2, the thermodynamics of the process change compared to heating under an inert atmosphere, and graphite does not take part in the reduction reaction.[31,33,34,59] The presence of excess O_2 during TGA/MS instead promotes the combustion of the organic material and graphite, resulting in the formation of CO_2 and CO, as shown by eqn (1)–(3).[34]

$$C_{(s)} + O_{2_{(g)}} \rightarrow CO_{2_{(g)}} \quad (1)$$

$$2C_{(s)} + O_{2_{(g)}} \rightarrow 2CO_{(g)} \quad (2)$$

$$2CO_{(s)} + O_{2_{(g)}} \rightarrow 2CO_{(g)} \quad (3)$$

Pristine commercial graphite reference is used to prepare a calibration curve by establishing a relation between the amount (mg) of graphite used in TGA and CO_2 gas detected by MS (integral of CO_2 MS spectrum), as shown in Fig. 4a and b. Fig. 4a shows the TG mass loss curves (left *y*-axis) and corresponding CO_2 MS spectra (right *y*-axis) for graphite reference at three different initial masses (4 mg, 8 mg, and 20 mg), where 100% mass loss is reached by ~850 °C and the only MS signal detected is for CO_2 gas. Fig. 4b shows that the initial mass of graphite reference is directly proportional to the integral of the CO_2 MS curve, whereby performing a linear fitting yields a correlation coefficient (R^2) of 99.8%. To quantify the carbon content (which is mainly graphite) in the BM samples using results obtained from Fig. 4a and b, eqn (4)–(7) have been established.

$$CO_2\ \text{MS curve integral} = m \times \text{Graphite mass} + c \quad (4)$$

$$m = 4.47858 \times 10^{-8}\ \text{A s mg}^{-1} \quad (5)$$

$$c = 1.47627 \times 10^{-9}\ \text{A s} \quad (6)$$

$$\text{Carbon (wt \%)} = \frac{(CO_2\text{MS integ.} - c)m}{\text{Initial mass of BM in TG (mg)}} \times 100 \quad (7)$$

Fig. 4c shows the TGA mass loss curves of the three BM samples, while Fig. 4d–f show the MS spectra of species (H_2O, CO_2, and CO) evolved from BM1, BM2, and BM3, respectively. The mass change in BM1, BM2, and BM3 within a temperature range of 50–300 °C under an inert atmosphere has already been discussed in the previous section, and the oxidative atmosphere in this case does not result in significant changes <300 °C. As the temperature reaches ~380 °C, the PVDF binder starts to decompose in all three BM samples, and complete removal of PVDF occurs at ~550 °C, as confirmed by TGA/MS analysis of pure PVDF in Fig. S5c and d. A significant change is that in the presence of excess O_2, the PVDF binder in BM samples is completely burned without leaving behind any carbonaceous char, as also shown by 100% mass loss in Fig. S5c and d. TGA/MS mass loss within 380–550 °C can be used to estimate the amount of PVDF (wt%) in BM.[58,60,61] The mass loss between the temperature range of 380–550 °C in Fig. 4c shows that BM1, BM2, and BM3 contain ~4.3 wt% PVDF binder. As the temperature increases above 550 °C, graphite and carbonaceous species start to combust instead of acting as a reducing agent due to the presence of excess O_2. The main product of the combustion process is CO_2 gas with relatively less formation of CO.

The integral of the CO_2 MS spectrum in Fig. 4d–f is calculated for BM1, BM2, and BM3, respectively, and eqn (7) is employed to calculate the carbon amount (wt%). It is important to note a key limitation of this method. While most of the graphite combusts to CO_2 under these excess oxygen conditions, the MS data confirm that a small fraction also forms CO gas. As the calibration curve and calculations are entirely based on the CO_2 signal, the graphite converted to CO is not accounted for. Consequently, this leads to a slight underestimation of the true total carbon content. Fig. 4g shows the calculated carbon amount (wt%) for BM samples as well as for pyrolyzed BM samples (TGA/MS data of pyrolyzed BM are shown in Fig. S7). The carbon content in BM1, BM2, and BM3 is determined to be 40.5 wt%, 40.6 wt% and 50.2 wt%, respectively. Fig. S6 compares the XRD patterns of the BM1 residue from oxidative and inert TGA/MS, where the residue from oxidative TGA/MS shows the NMC crystalline peaks and complete combustion of graphite. This confirms that, under oxidative TGA/MS, graphite oxidizes completely and can thus be accurately quantified by the developed method. Fig. 4h shows the carbon content (wt%) in the four sieved fractions (+150 μm, −150 + 90 μm, −90 + 63 μm, and −63 μm) of BM1, calculated by applying the developed method on TGA/MS analyses of each sieved fraction (shown in Fig. S8). Fig. 4h implies that the carbon is primarily concentrated in the

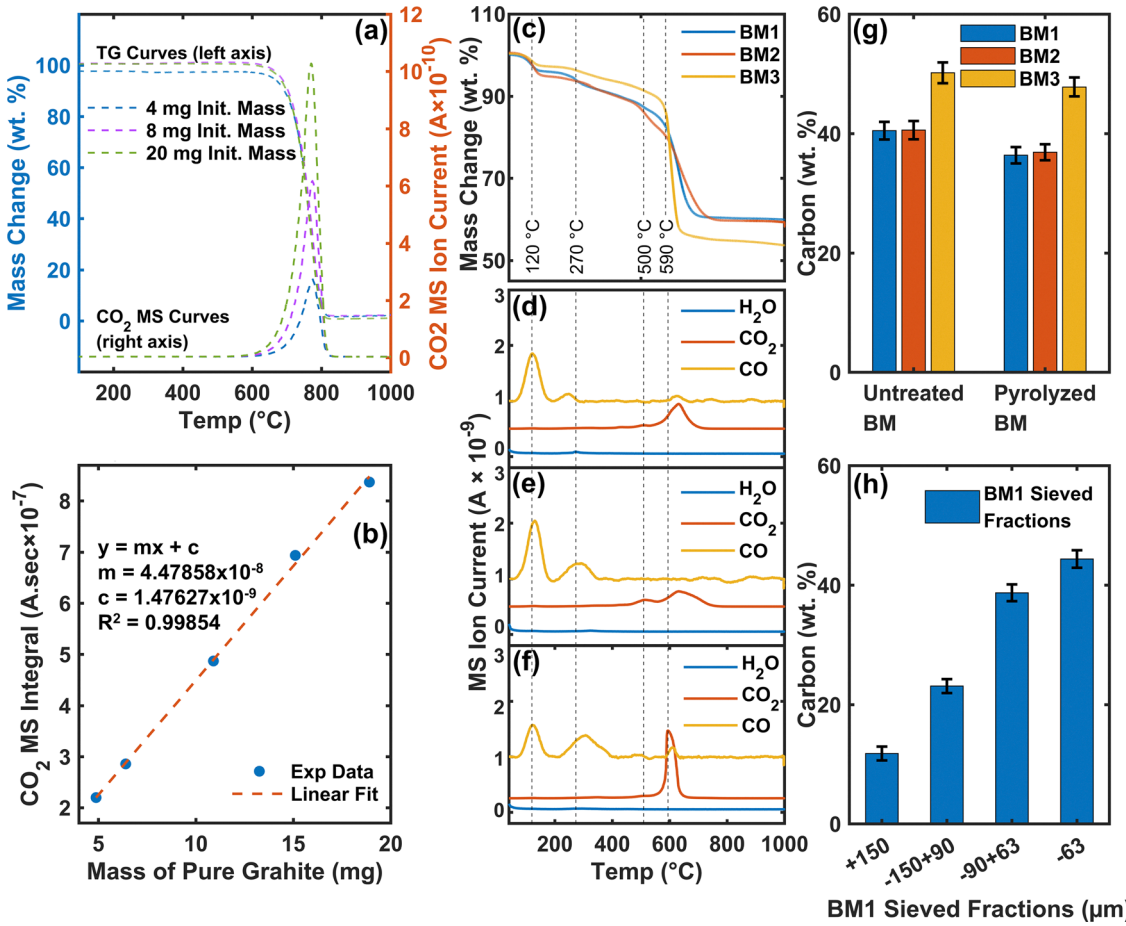

Fig. 4 Use of TGA + MS for quantification of the total carbon content in the three BM samples (BM1, BM2, BM3) by developing a calibration curve using pure graphite as a reference, (a) TG curves on the left *y*-axis and CO_2 MS curves on the right *y*-axis for pure graphite reference at three different initial masses (4 mg, 8 mg, and 20 mg), (b) linear fit to develop calibration curve using the integral of CO_2 MS curves as a function of initial graphite mass, (c) TG mass change curves for the three BM samples (BM1, BM2, BM3), (d) H_2O, CO_2 and CO MS curves for BM1, (e) H_2O, CO_2 and CO MS curves for BM2, (f) H_2O, CO_2 and CO MS curves for BM3, (g) measured carbon (wt%) for untreated BM samples as well as pyrolyzed BM samples based on the prepared calibration curve and (h) shows the distribution of total carbon (wt%) within sieved fractions of BM1.

medium-size (−90 + 63 µm) and finer-size (−63 µm) fractions of the BM1 sample.

Surface morphology and structural order

SEM/EDS can be employed as a complementary technique for the local investigation of the surface properties of BM particles. Fig. 5 shows the SEM images and energy dispersive X-ray (EDX) analysis of the three BM samples, where the particles can be distinctively categorized into two types based on their morphological features: graphite anode particles and NMC cathode particles. Fig. 5a, c and e show the SEM images of graphite particles for BM1, BM2, and BM3, respectively. These graphite particles for all three BM samples are irregular-shaped and have a slightly rough morphology with deposition of small brighter particles on the surface, which are primarily transition metals, *i.e.*, Ni, Mn, and Co (as shown by the EDX analysis in Fig. S9). Fig. 5b, d, and f show the SEM images of NMC particles for BM1, BM2, and BM3, respectively. The surface morphology of NMC particles is more defined, revealing small needle-like structures. The presence of these needle-like structures is an indication that the cathode particle is intact and present in the form of $Li[Ni_xMn_yCo_z]O_2$.[62]

Fig. 5g shows the EDX analysis of an NMC particle for BM1, where the surface primarily consists of Ni (38.7 wt%), Mn (10.1 wt%), and Co (12.4 wt%). A molar ratio between Ni, Mn, and Co amounts for BM1 (Fig. 5g) demonstrates that this is NMC622, which is in line with the metal composition data (Table 1). Similarly, Fig. 5h and i show the EDX analysis of BM2 and BM3, respectively. Here, a molar ratio between Ni:Mn:Co shows NMC111 for BM2 and NMC901 for BM3, which is again in agreement with Table 1. EDX mapping of fluorine on the surface of active particles is of particular interest as it is a direct visualization of PVDF binder distribution.[7] Several factors can complicate the accurate mapping of fluorinated binders in LIB cathodes, requiring careful analysis and mitigating strategies. Fluorine emits relatively low-energy Kα X-rays and is difficult to differentiate from transition metals due to their similar Kα X-ray energies.[63] This spectral overlap, combined with the fact that the amount of fluorine-containing species (*e.g.*, PVDF) in BM samples is significantly lower than the amount of transition

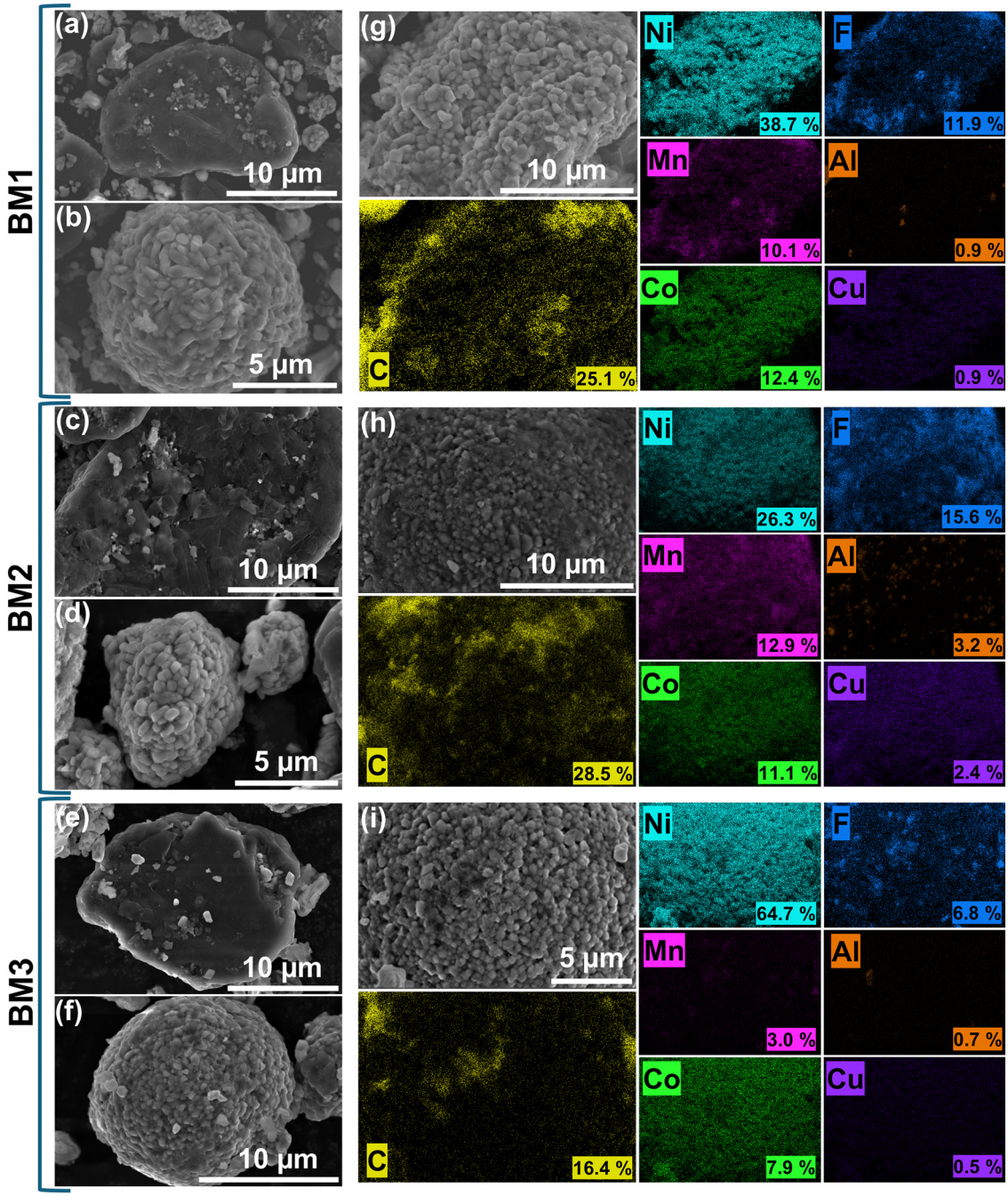

Fig. 5 SEM imaging and EDX analysis of the three BM samples. (a) and (b) SEM images of BM1, (c) and (d) SEM images of BM2, (e) and (f) SEM images of BM3, (g) EDX analysis of BM1, (h) EDX analysis of BM2, and (i) EDX analysis of BM3.

metals, means fluorine X-rays constitute a minimal fraction of the total X-ray emissions.[63] Furthermore, fluorine is highly electronegative, and long/repeated exposure to the electron beam can induce fluorine mobility, where fluorine migrates from fluorine-rich zones to fluorine-free zones, causing unrealistic surface changes.[63] To mitigate these challenges, the EDX mapping was performed at a low accelerating voltage (5–7 kV), drastically reducing the electron interaction volume, which has been shown to improve the spatial resolution of fluorine EDX maps.[63] Additionally, the use of a modern, large-area silicon drift detector used in this study provides the high spectral resolution and sensitivity necessary to effectively deconvolute the weak fluorine signal from the strong, overlapping peaks of the transition metals. Fig. 5g–i also show that a relatively higher amount of fluorine is present on the surface of NMC cathode particles for BM1 (11.9 wt%), BM2 (15.6 wt%), and BM3 (6.8 wt%) compared to graphite anode particles (Fig. S9). SEM images and EDX analysis of BM samples after pyrolysis show a significant morphological change for NMC particles due to being reduced to metal oxides and metallic phases (shown in

Fig. S10). EDX analyses of pyrolyzed BM1 (Fig. S10g), BM2 (Fig. S10h), and BM3 (Fig. S10i) show that the fluorine content (wt%) on the surface of NMC particles has significantly decreased (1.7–2.4 wt%), due to the decomposition of the PVDF binder during the pyrolysis pre-treatment.

The surface properties of graphite particles can be examined more comprehensively using Raman spectroscopy, as it can reveal valuable information related to surface depositions and structural defects in graphite particles.[18] Fig. 6 shows the Raman spectra of various surface spots for BM2, where the spectra are classified into two types: spectra from high-reflectance spots under the microscope shown in Fig. 6a and spectra from low-reflectance spots shown in Fig. 6b. Fig. 6a shows three Raman spectra on three different surface spots for the BM2 sample surface, where three main carbon peaks are identified. In Fig. 6a, the first peak appearing at ~1350–1351 cm^{-1} is referred to as the D-band (disordered band) and is attributed to in-plane defects in the polyaromatic layers or the edge of the sp^2 graphene plane.[64] The next peak, which is relatively intense in all three spectra of Fig. 6a, called the G-band (graphitic band), appears at 1580–1600 cm^{-1}. The G-band is reported to be associated with the stretching vibration of aromatic rings and the crystal structure of sp^2 carbon atoms.[65] A very minor peak, which appears as a shoulder of the G-band at ~1620 cm^{-1}, is labeled as the D′-band. This D′-band occurs from a similar mechanism to the D-band.[65] Fig. 6b shows that Raman spectra of the low-reflectance spots give rise to 5 disordered bands (D*, D, D″, and D′) and a G-band. The D*-band appears at ~1200 cm^{-1} and is attributed to the sp^3 structure and sp^2–sp^3 hybrid carbon near the microcrystal.[65] The D* and D″ bands can be attributed to amorphous and impurity contributions.[66]

An important spectral feature when investigating carbonaceous samples is the I_D/I_G ratio, *i.e.*, the ratio of the intensity of the D-band to that of the G-band. The results show that the high-reflectance spectra in Fig. 6a (spectra 1, 2, and 3) exhibit a very low I_D/I_G ratio of ~0.1, while the low-reflectance spectra in Fig. 6b (spectra 4, 5, and 6) show a relatively higher I_D/I_G ratio of ~1.0. A higher I_D/I_G value points to the existence of more defects and surface deposition on the spots where spectra 4, 5, and 6 are captured.[67] This, together with the presence of D* and D″ in these spectra, suggests that the surface of scanned particles in spectra 4, 5, and 6 could be covered with a layer of disordered carbon.[68]

Importance of characterization in guiding recycling strategies

The goal of this study is to create a characterization framework, which employs a combination of characterization techniques, as a guide to develop efficient recycling processes that maximize the recovery of all valuables in the analyzed BM samples, where BM1, BM2, and BM3 belong to NMC622, NMC111, and NMC901 chemistries (shown by XRD patterns in Fig. 2 and mass composition data in Table 1). Fig. 7 shows a visual summary of this characterization framework, where the innermost ring shows the techniques used in this study. Each subsequent layer moves outward to specify the primary purpose

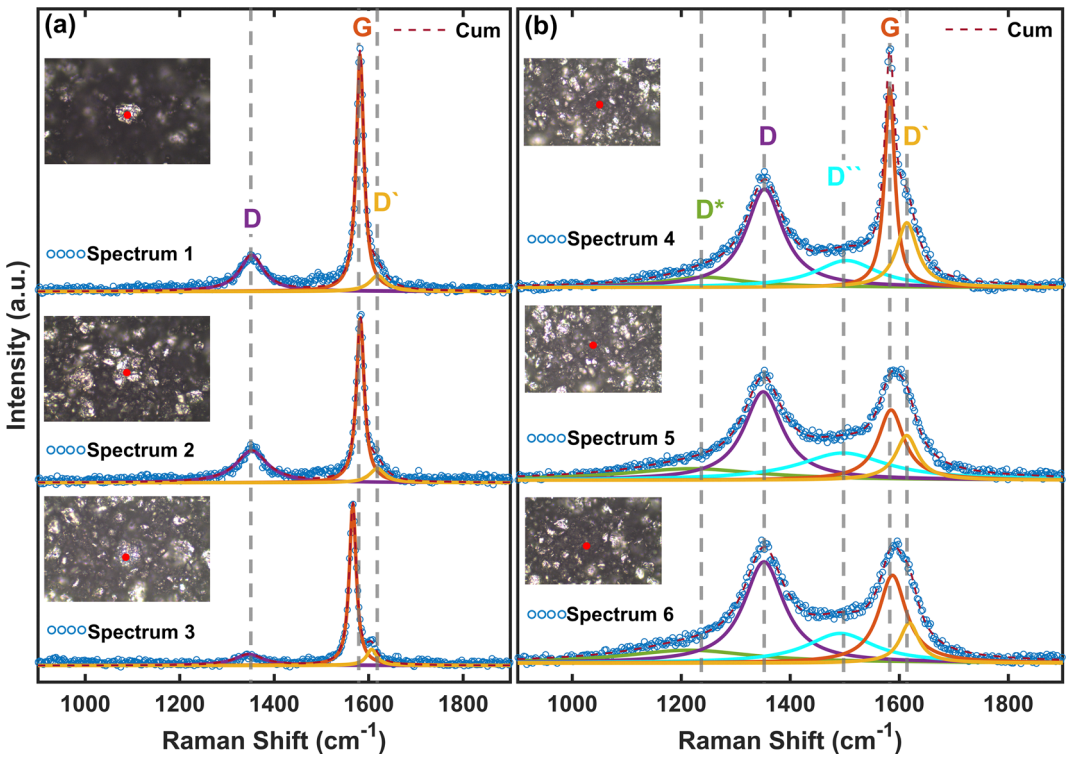

Fig. 6 Raman spectra and fitting profiles for various surface spots of the BM2 sample. (a) The three spectra where three 1st-order carbonaceous peaks are detected. (b) The three spectra where 5 carbonaceous peaks are detected.

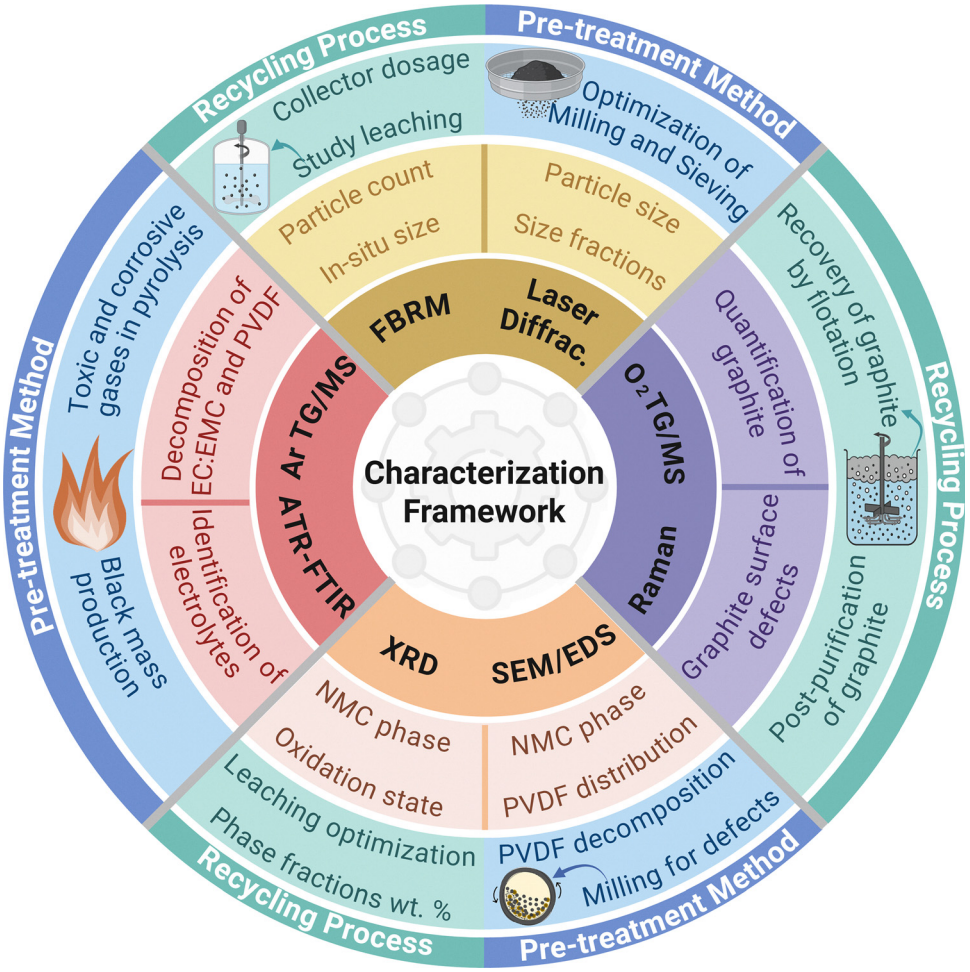

Fig. 7 Illustration of the created characterization framework for optimizing BM pre-treatment and recycling processes. The framework connects each characterization technique to its primary objective and its specific role in optimizing pre-treatment and recycling processes.

of each technique, its direct application, and finally, its relevance. A primary challenge in recycling is the inherent heterogeneity of BM, demonstrated by PSD (Fig. 1a), CLD (Fig. 1b-c), sieve analysis (Fig. 1d), and metal composition data across different sieved fractions (Fig. 1f). Previous studies have shown that particle size has a direct effect on the efficiency of hydrometallurgical recycling processes (such as leaching and froth flotation), where finer BM particles, with their higher specific surface area, improve metal leaching efficiency.[69] However, in froth flotation, finer particles reduce graphite purity due to entrainment.[70] These challenges can be overcome by sieving BM into different size fractions (Fig. 1), where the smallest size fraction (−63 μm), with its high specific surface area, can be subjected to leaching for enhanced metal recovery. However, the mid-size fraction can be used in the flotation process, minimizing the entrainment of fine particles that would otherwise reduce graphite purity. Additionally, froth flotation of the mid-size fraction would also up-concentrate the metals in the flotation underflow (tailings), thus lowering overall leaching reagent demand.[71] Furthermore, XRD analysis revealed that the NMC particles in all BM samples are highly crystalline, suggesting slow leaching kinetics due to their well-ordered layered structure. These findings suggest that introducing lattice disorder in the NMC crystal structure by mechanical pre-treatment (*e.g.*, milling) can be an additional step to enhance the leaching efficiency of Ni, Co, and Mn from NMC.[56]

Another major challenge in recycling BM is the PVDF binder, which is inert, hydrophobic, and deposited on the active particle surface, hindering leaching efficiency,[58] and the separation of graphite *via* froth flotation.[21] QPA of XRD patterns (Fig. 2) using the internal standard method revealed 8–11 wt% amorphous content in BM samples, which partially consist of the PVDF binder and other organic species. SEM/EDS analysis (Fig. 5) provided direct visual confirmation, mapping the distribution of fluorine on the surface of NMC cathode particles and thereby visualizing the PVDF coating. A widely reported method to remove this PVDF binder coating is pyrolysis pre-treatment, which can decompose the binder into carbonaceous and fluorinated gases. TGA/MS analysis under pyrolytic conditions (Fig. 3) provides a detailed understanding of the pyrolysis pre-treatment by identifying the evolution of

electrolytes at lower temperatures and the decomposition of PVDF between 380 °C and 500 °C (Fig. 3). Critically, this analysis reveals the evolution of carbonaceous and fluorinated gases and traces them back to the originating species.

The pre-treated BM feed can now be subjected to hydrometallurgical recycling processes. For leaching processes (*e.g.*, selective water-leaching of Li from pyrolyzed BM and subsequent total acid leaching of the finest fraction), the developed FBRM method offers a significant advantage. The developed FBRM method (Fig. 1) correlates the chord length of BM particles measured using the FBRM method with the particle size measured using the laser diffraction technique. The developed method allows real-time measurement of particle size (as chord length) during pre-treatment and recycling processes. In a leaching process flow, an FBRM probe could continuously track the dissolution of NMC particles, providing real-time data on leaching kinetics without offline sampling. Here, the insights gained from XRD phase identification (Fig. 2) and metal composition data (Table 1) regarding NMC chemistry can be used for calculating the stoichiometric amount of the leaching reagent as well as reducing reagent required for the effective dissolution of transition metals from their higher oxidation states to their more soluble forms (Ni^{2+}, Mn^{2+}, Co^{2+}). Furthermore, a significant challenge in hydrometallurgical processes (*e.g.*, leaching) is the contamination of aqueous streams with fluoride ions, which originate primarily from the hydrolysis of the residual electrolyte salt, $LiPF_6$.[72,73] To mitigate fluorine-related environmental concerns,[59] future studies should employ IC (Ion Chromatography) for tracking and quantifying fluoride in leachates and process waters.

Finally, the recycling process flow aimed at recovering graphite from BM by flotation of the mid-size fraction can also benefit from the developed characterization methods. For instance, Wang *et al.* used FBRM to enhance fine-coal flotation,[74] and Haung *et al.* employed it to optimize collector dosage.[45] In graphite flotation from BM, a similar methodology can be applied to optimize process parameters, such as the kerosene collector dosage, by monitoring particle aggregation using FBRM. Additionally, zeta potential and contact angle of graphite and the NMC cathode in a BM sample should also be investigated in a future study, since these parameters can guide the selection of pH, water chemistry and collector dosage during froth flotation. A novel oxidative TGA/MS method developed in this study can be used to quantify the graphite content in BM (Fig. 4). This method is valuable for pre-treatment and recycling processes, such as pyrolysis and froth flotation, that are influenced by the amount of graphite. To further understand the quality of the carbonaceous material, peak fitting of Raman spectra offers detailed insights into the changes in structural order of graphite particles caused by defects and surface depositions (Fig. 6). The analysis of I_D/I_G ratios revealed the heterogeneous nature of graphite particle surfaces, with higher ratios indicating the presence of surface depositions and disordered carbon. This information can further guide the development of purification steps needed to achieve battery-grade graphite from the recycled concentrate. In addition to the structural data from Raman spectroscopy, future work could employ BET (Brunauer–Emmett–Teller) analysis to measure the specific surface area of the recovered graphite, a critical parameter for evaluating its performance in new battery anodes. By integrating the studied characterization techniques, a comprehensive, data-driven framework is established (Fig. 7), enabling the design of optimized recycling strategies that can adapt to the complex and heterogeneous nature of BM feed.

Conclusions

This study has thoroughly investigated the physicochemical properties of three BM samples obtained from NMC-based end-of-life LIBs to determine their implications for pre-treatment and recycling processes. Furthermore, this study underscores the significant heterogeneity inherent in black mass. To ensure the reliability and comparability of characterization data in the future, the development of standardized sampling protocols is strongly recommended. A method for measuring the particle size of BM as chord length using the FBRM technique has been developed by applying square-weighing to the CLD data. This allows real-time measurement of the particle size as chord length. XRD patterns of BM confirmed that the crystalline NMC and graphite phases are well-preserved, which, combined with the metal composition data, showed that BM1, BM2, and BM3 belong to NMC622, NMC111, and NMC901 chemistries. Furthermore, the QPA of XRD patterns using Rietveld refinement and the internal standard method showed the wt% of crystalline and amorphous phases in each BM sample. SEM/EDS analysis revealed the deposition of metals on the surface of graphite particles as well as the distribution of the PVDF binder on NMC particles by detecting fluorine. TGA/MS under pyrolytic conditions showed that the decomposition of PVDF and other species in BM produces carbonaceous (CO_2, CO, and CH_4) and fluorinated (HF and fluorine) gases.

A novel finding of this study is the quantification of graphite as total carbon in NMC-based BM using a calibration curve developed with TGA/MS of pure graphite under oxidative conditions. Oxidative TGA/MS is also used to estimate the amount of PVDF in BM. Graphite particles in BM were studied using Raman spectroscopy, and the results showed that I_D/I_G ratios varied across the surface in the same BM sample due to deposition of carbonaceous species on graphite. Overall, this study highlights the importance of linking various characterization techniques, where the insights gained into chord length measurement, particle size effects, quantitative phase analysis, PVDF deposition, binder removal, and carbon quantification provide a framework for optimizing recycling strategies that maximize recovery of valuables in BM.

Author contributions

Hammad Farooq: methodology, formal analysis, investigation, data curation, writing – original draft, visualization, and conceptualization. Sulalit Bandyopadhyay: conceptualization,

writing – review and editing, supervision, project administration, and funding acquisition.

Conflicts of interest

The authors declare that they have no known competing financial interests or personal relationships that could have appeared to influence the work reported in this paper.

Data availability

Supplementary information is available. See DOI: https://doi.org/10.1039/d5ma00545k.

Acknowledgements

This work was carried out as part of the SUMBAT (Sustainable Materials for the Battery Value Chain) project, funded by the Research Council of Norway, Innovation Norway, and SIVA (Industrial Development Corporation of Norway) under the Norwegian Green Platform Initiative. The authors also acknowledge the support of the Norwegian Micro- and Nano-Fabrication Facility (NorFab).

References

1 F. Degen, M. Winter, D. Bendig and J. Tübke, Energy consumption of current and future production of lithium-ion and post lithium-ion battery cells, *Nat. Energy*, 2023, **8**(11), 1284–1295, DOI: 10.1038/s41560-023-01355-z.

2 European Commission. Joint Research Centre., Li-ion batteries for mobility and stationary storage applications: scenarios for costs and market growth. LU: Publications Office, 2018. Accessed: Feb. 03, 2025. [Online]. Available: https://data.europa.eu/doi/10.2760/87175.

3 *The battery industry has entered a new phase – Analysis*, IEA. Accessed: July 17, 2025. [Online]. Available: https://www.iea.org/commentaries/the-battery-industry-has-entered-a-new-phase.

4 J. A. Llamas-Orozco, *et al.*, Estimating the environmental impacts of global lithium-ion battery supply chain: a temporal, geographical, and technological perspective, *PNAS Nexus*, 2023, **2**(11), pgad361, DOI: 10.1093/pnasnexus/pgad361.

5 E. Commission, E. Directorate-General for Internal Market Industry, SMEs, M. Grohol, and C. Veeh, Study on the critical raw materials for the EU 2023 – Final report. Publications Office of the European Union, 2023, DOI: 10.2873/725585.

6 Regulation (EU) 2023/1542 of the European Parliament and of the Council of 12 July 2023 concerning batteries and waste batteries. July 12, 2023. Accessed: July 24, 2025. [Online]. Available: https://data.europa.eu/eli/reg/2023/1542/2024-07-18.

7 M. Wang, *et al.*, Challenges in recycling spent lithium-ion batteries: spotlight on polyvinylidene fluoride removal, *Global Challenges*, 2023, **7**(3), 2200237, DOI: 10.1002/gch2.202200237.

8 S. D. Widijatmoko, F. Gu, Z. Wang and P. Hall, Selective liberation in dry milled spent lithium-ion batteries, *Sustainable Mater.Technol.*, 2020, **23**, e00134, DOI: 10.1016/j.susmat.2019.e00134.

9 A. Vanderbruggen, A. Salces, A. Ferreira, M. Rudolph and R. Serna-Guerrero, Improving separation efficiency in end-of-life lithium-ion batteries flotation using attrition pre-treatment, *Minerals*, 2022, **12**(1), 1, DOI: 10.3390/min12010072.

10 S. Windisch-Kern, *et al.*, Recycling chains for lithium-ion batteries: A critical examination of current challenges, opportunities and process dependencies, *Waste Manage.*, 2022, **138**, 125–139, DOI: 10.1016/j.wasman.2021.11.038.

11 S. Doose, J. K. Mayer, P. Michalowski and A. Kwade, Challenges in Ecofriendly Battery Recycling and Closed Material Cycles: A Perspective on Future Lithium Battery Generations, *Metals*, 2021, **11**(2), 2, DOI: 10.3390/met11020291.

12 C. Wilke, D. M. Werner, A. Kaas and U. A. Peuker, Influence of the crusher settings and a thermal pre-treatment on the properties of the fine fraction (black mass) from mechanical lithium-ion battery recycling, *Batteries*, 2023, **9**(10), 10, DOI: 10.3390/batteries9100514.

13 J. Biswas, S. Ulmala, X. Wan, J. Partinen, M. Lundström and A. Jokilaakso, Selective sulfation roasting for cobalt and lithium extraction from industrial LCO-rich spent black mass, *Metals*, 2023, **13**(2), 2, DOI: 10.3390/met13020358.

14 O. Renier, A. Pellini and J. Spooren, Advances in the separation of graphite from lithium iron phosphate from end-of-life batteries shredded fine fraction using simple froth flotation, *Batteries*, 2023, **9**(12), 589, DOI: 10.3390/batteries9120589.

15 T. Rinne, N. Araya-Gómez and R. Serna-Guerrero, A study on the effect of particle size on Li-ion battery recycling via flotation and perspectives on selective flocculation, *Batteries*, 2023, **9**(2), 68, DOI: 10.3390/batteries9020068.

16 M. Muhaimin, A. Y. Chaerunisaa and R. Bodmeier, Real-time particle size analysis using focused beam reflectance measurement as a process analytical technology tool for continuous microencapsulation process, *Sci. Rep.*, 2021, **11**(1), 19390, DOI: 10.1038/s41598-021-98984-9.

17 C. Badenhorst, *et al.*, Recovery of graphite from spent lithium-ion batteries, *Recycling*, 2023, **8**(5), 5, DOI: 10.3390/recycling8050079.

18 E. Mousa, *et al.*, Characterization and thermal treatment of the black mass from spent lithium-ion batteries, *Sustainability*, 2022, **15**(1), 1, DOI: 10.3390/su15010015.

19 H. Wang, C. Liu, G. Qu, S. Zhou, B. Li and Y. Wei, Study on pyrolysis pretreatment characteristics of spent lithium-ion batteries, *Separations*, 2023, **10**(4), 4, DOI: 10.3390/separations10040259.

20 M. Abdollahifar, S. Doose, H. Cavers and A. Kwade, Graphite recycling from end-of-life lithium-ion batteries: processes

and applications, *Adv. Mater. Technol.*, 2023, **8**(2), 2200368, DOI: **10.1002/admt.202200368**.

21 J. Li, J. Zhang, W. Zhao, D. Lu, G. Ren and Y. Tu, Application of roasting flotation technology to enrich valuable metals from spent $LiFePO_4$ batteries, *ACS Omega*, 2022, **7**(29), 25590–25599, DOI: **10.1021/acsomega.2c02764**.

22 L. Donnelly, *et al.*, The recycling of end-of-life lithium-ion batteries and the phase characterisation of black mass, *Recycling*, 2023, **8**(4), 59, DOI: **10.3390/recycling8040059**.

23 G. Hong, H. Park, A. Gomez-Flores, H. Kim, J. Mi Lee and J. Lee, Direct flotation separation of active materials from the black mass of lithium nickel cobalt manganese oxides-type spent lithium-ion batteries, *Separation and Purification Technology*, Elsevier B. V., vol. 336, p. 126327, 2024. , DOI: **10.1016/j.seppur.2024.126327**.

24 S. Zhou, *et al.*, A comparative study on the influence of single and combined ultrasounds assisted flake graphite flotation, *Ultrasonics Sonochemistry*, Elsevier B. V., vol. 99, p. 106551, 2023, DOI: **10.1016/j.ultsonch.2023.106551**.

25 S. Nazari, *et al.*, Effect of roasting pretreatment on micro-nanobubble-assisted flotation of spent lithium-ion batteries, *J. Mater. Res. Technol.*, 2023, **24**, 2113–2128, DOI: **10.1016/j.jmrt.2023.03.133**.

26 T.-O. Folayan, A. L. Lipson, J. L. Durham, H. Pinegar, D. Liu and L. Pan, Direct recycling of blended cathode materials by froth flotation, *Energy Technol.*, 2021, **9**(10), 2100468, DOI: **10.1002/ente.202100468**.

27 H. Yu, *et al.*, Mechanistic insights into the lattice reconfiguration of the anode graphite recycled from spent high-power lithium-ion batteries, *J. Power Sources*, 2021, **481**, 229159, DOI: **10.1016/j.jpowsour.2020.229159**.

28 G. R. A. Kumara, *et al.*, Development of a chemical-free floatation technology for the purification of vein graphite and characterization of the products, *Sci. Rep.*, 2021, **11**(1), 1, DOI: **10.1038/s41598-021-02101-9**.

29 C. Wang, *et al.*, Enhancement on the selective flotation separation of carbon coated $LiFePO_4$ and graphite electrode materials, *Sep. Purif. Technol.*, 2023, **311**, 123252, DOI: **10.1016/j.seppur.2023.123252**.

30 Y. Gao, *et al.*, Graphite recycling from the spent lithium-ion batteries by sulfuric acid curing–leaching combined with high-temperature calcination, *ACS Sustainable Chem. Eng.*, 2020, **8**(25), 9447–9455, DOI: **10.1021/acssuschemeng.0c02321**.

31 R. Tao, *et al.*, Kinetics study and recycling strategies in different stages of full-component pyrolysis of spent LiNixCoyMnzO2 lithium-ion batteries, *Waste Manage.*, 2023, **155**, 8–18, DOI: **10.1016/j.wasman.2022.10.033**.

32 H. Huang, C. Liu and Z. Sun, Transformation and migration mechanism of fluorine-containing pollutants in the pyrolysis process of spent lithium-ion battery, *J. Hazard. Mater.*, 2022, **435**, 128974, DOI: **10.1016/j.jhazmat.2022.128974**.

33 C. Stallmeister and B. Friedrich, Influence of flow-gas composition on reaction products of thermally treated NMC battery black mass, *Metals*, 2023, **13**(5), 5, DOI: **10.3390/met13050923**.

34 G. Lombardo, B. Ebin, B.-M. Steenari, M. Alemrajabi, I. Karlsson and M. Petranikova, Comparison of the effects of incineration, vacuum pyrolysis and dynamic pyrolysis on the composition of NMC-lithium battery cathode-material production scraps and separation of the current collector, *Resour., Conserv. Recycl.*, 2021, **164**, 105142, DOI: **10.1016/j.resconrec.2020.105142**.

35 R. Zhan, Z. Oldenburg and L. Pan, Recovery of active cathode materials from lithium-ion batteries using froth flotation, *Sustainable Mater. Technol.*, 2018, **17**, e00062, DOI: **10.1016/j.susmat.2018.e00062**.

36 X. Ma, M. Chen, B. Chen, Z. Meng and Y. Wang, High-performance graphite recovered from spent lithium-ion batteries, *ACS Sustainable Chem. Eng.*, 2019, **7**(24), 19732–19738, DOI: **10.1021/acssuschemeng.9b05003**.

37 H. Wang, *et al.*, Reclaiming graphite from spent lithium ion batteries ecologically and economically, *Electrochim. Acta*, 2019, **313**, 423–431, DOI: **10.1016/j.electacta.2019.05.050**.

38 X. Xiao, *et al.*, Ultrasound-assisted extraction of metals from lithium-ion batteries using natural organic acids, *Green Chem.*, 2021, **23**(21), 8519–8532, DOI: **10.1039/D1GC02693C**.

39 J. Han, L. Chen, X. Zhong, X. Wei and W. Qin, A promising method for recovery of LiMn2O4 and graphite from waste lithium-ion batteries: roasting enhanced flotation, *J. Cent. South Univ.*, 2022, **29**(9), 2873–2887, DOI: **10.1007/s11771-022-5127-1**.

40 A. R. Heath, P. D. Fawell, P. A. Bahri and J. D. Swift, Estimating average particle size by focused beam reflectance measurement (FBRM), *Part. Part. Syst. Char.*, 2002, **19**(2), 84, DOI: **10.1002/1521-4117(200205)19:2%3C84::AID-PPSC84%3E3.0.CO;2-1**.

41 M. Wojdyr, *Fityk*: a general-purpose peak fitting program, *J. Appl. Crystallogr.*, 2010, **43**(5), 1126–1128, DOI: **10.1107/S0021889810030499**.

42 S. Andrews, D. Nover and S. G. Schladow, Using laser diffraction data to obtain accurate particle size distributions: the role of particle composition, *Limnol. Oceanogr. Methods*, 2010, **8**(10), 507–526, DOI: **10.4319/lom.2010.8.507**.

43 P. Hu, L. Liang, B. Li and W. Xia, Delving into the heterocoagulation between coal and quartz at different shear rates by the focused beam reflectance measurement (FBRM) and particle vision and measurement (PVM) techniques, *Fuel*, 2021, **286**, 119445, DOI: **10.1016/j.fuel.2020.119445**.

44 A. F. Grabsch, M. Yahyaei and P. D. Fawell, Number-sensitive particle size measurements for monitoring flocculation responses to different grinding conditions, *Miner. Eng.*, 2020, **145**, 106088, DOI: **10.1016/j.mineng.2019.106088**.

45 G. Huang, Z. Yang, Y. Zhao, X. Sun, B. Yang and L. Wang, Impact of power input in pulp conditioning on coal flotation and real-time characterization by focused beam reflectance measurement (FBRM), *Energy Sources Part A*, 2024, **46**(1), 10078–10091, DOI: **10.1080/15567036.2024.2382917**.

46 H. Li, M. A. Grover, Y. Kawajiri and R. W. Rousseau, Development of an empirical method relating crystal size distributions and FBRM measurements, *Chem. Eng. Sci.*, 2013, **89**, 142–151, DOI: **10.1016/j.ces.2012.10.031**.

47 W. Yu and K. Erickson, Chord length characterization using focused beam reflectance measurement probe - methodologies and pitfalls, *Powder Technol.*, 2008, **185**(1), 24–30, DOI: 10.1016/j.powtec.2007.09.011.

48 R. Jung, M. Metzger, F. Maglia, C. Stinner and H. A. Gasteiger, Chemical versus Electrochemical Electrolyte Oxidation on NMC111, NMC622, NMC811, LNMO, and Conductive Carbon, *J. Phys. Chem. Lett.*, 2017, **8**(19), 4820–4825, DOI: 10.1021/acs.jpclett.7b01927.

49 D. McNulty, A. Hennessy, M. Li, E. Armstrong and K. M. Ryan, A review of Li-ion batteries for autonomous mobile robots: Perspectives and outlook for the future, *J. Power Sources*, 2022, **545**, 231943, DOI: 10.1016/j.jpowsour.2022.231943.

50 A. Manthiram, J. C. Knight, S.-T. Myung, S.-M. Oh and Y.-K. Sun, Nickel-Rich and Lithium-Rich Layered Oxide Cathodes: Progress and Perspectives, *Adv. Energy Mater.*, 2016, **6**(1), 1501010, DOI: 10.1002/aenm.201501010.

51 L. Li, Q. Ran, Q. Hu, Y. Ji and X. Liu, Enabling high nickel LiNi0.9Co0.1O2 cathode with enhanced cycling performance at high temperature by a phospholipid-like protective layer, *J. Alloys Compd.*, 2023, **953**, 170032, DOI: 10.1016/j.jallcom.2023.170032.

52 A. C. Martinez, *et al.*, High reactivity of the nickel-rich LiNi1-x-yMnxCoyO2 layered materials surface towards H2O/CO2 atmosphere and LiPF6-based electrolyte, *J. Power Sources*, 2020, **468**, 228204, DOI: 10.1016/j.jpowsour.2020.228204.

53 J. Choi, L. Dong, C.-Y. Yu, C. O'Meara, E. Lee and J.-H. Kim, Relationship of Chemical Composition and Moisture Sensitivity in LiNixMnyCo1−X−YO2 for Lithium-Ion Batteries, *J. Electrochem. Energy Con. Storage*, 2021, **18**, 041009, DOI: 10.1115/1.4051208.

54 W. Xuan, A. Otsuki and A. Chagnes, Investigation of the leaching mechanism of NMC 811 (LiNi 0.8 Mn 0.1 Co 0.1 O 2) by hydrochloric acid for recycling lithium ion battery cathodes, *RSC Adv.*, 2019, **9**(66), 38612–38618, DOI: 10.1039/C9RA06686A.

55 N. Vieceli, P. Benjamasutin, R. Promphan, P. Hellström, M. Paulsson and M. Petranikova, Recycling of Lithium-Ion Batteries: Effect of Hydrogen Peroxide and a Dosing Method on the Leaching of LCO, NMC Oxides, and Industrial Black Mass, *ACS Sustainable Chem. Eng.*, 2023, **11**(26), 9662–9673, DOI: 10.1021/acssuschemeng.3c01238.

56 L. Lv, *et al.*, Recycling and Reuse of Spent LIBs: Technological Advances and Future Directions, *Molecules*, 2024, **29**(13), 3161, DOI: 10.3390/molecules29133161.

57 B. Cagnon, D. Daval, M. Cabié, D. Lemarchand and S. Gin, A comparative study of the dissolution mechanisms of amorphous and crystalline feldspars at acidic pH conditions, *npj Mater. Degrad.*, 2022, **6**(1), 34, DOI: 10.1038/s41529-022-00240-6.

58 R. Golmohammadzadeh, *et al.*, Removal of polyvinylidene fluoride binder and other organics for enhancing the leaching efficiency of lithium and cobalt from black mass, *J. Environ. Manage.*, 2023, **343**, 118205, DOI: 10.1016/j.jenvman.2023.118205.

59 G. Lombardo, B. Ebin, M. R. St. J. Foreman, B.-M. Steenari and M. Petranikova, Incineration of EV lithium-ion batteries as a pretreatment for recycling – determination of the potential formation of hazardous by-products and effects on metal compounds, *J. Hazard. Mater.*, 2020, **393**, 122372, DOI: 10.1016/j.jhazmat.2020.122372.

60 G. Jiang, D. Lee, D. Raimbault, P. A. Anderson and G. A. Leeke, Acetone as an agent for PVDF recovery and delamination of lithium-ion battery electrodes, *Resour., Conserv. Recycl.*, 2024, **209**, 107778, DOI: 10.1016/j.resconrec.2024.107778.

61 R. Zhan, Z. Yang, I. Bloom and L. Pan, Significance of a Solid Electrolyte Interphase on Separation of Anode and Cathode Materials from Spent Li-Ion Batteries by Froth Flotation, *ACS Sustainable Chem. Eng.*, 2021, **9**(1), 531–540, DOI: 10.1021/acssuschemeng.0c07965.

62 A. C. Martinez, *et al.*, High reactivity of the nickel-rich LiNi1-x-yMnxCoyO2 layered materials surface towards H2O/CO2 atmosphere and LiPF6-based electrolyte, *J. Power Sources*, 2020, **468**, 228204, DOI: 10.1016/j.jpowsour.2020.228204.

63 J. Parker, R. Smith and D. Cumming, High-Resolution X-ray Mapping of Fluorinated Binders in Lithium-Ion Battery Electrodes, *J. Phys. Chem. C*, 2024, **128**(49), 20957–20966, DOI: 10.1021/acs.jpcc.4c05678.

64 J. Li, Y. Qin, Y. Chen and J. Shen, Microstructural characteristics of graphite microcrystals in graphitized coal: insights from petrology, mineralogy and spectroscopy, *Minerals*, 2022, **12**(10), 10, DOI: 10.3390/min12101189.

65 Y. Yin, *et al.*, Effect of char structure evolution during pyrolysis on combustion characteristics and kinetics of waste biomass, *J. Energy Res. Technol.*, 2018, **140**(7), 72203, DOI: 10.1115/1.4039445.

66 Z. E. Brubaker, J. J. Langford, R. J. Kapsimalis and J. L. Niedziela, Quantitative analysis of raman spectral parameters for carbon fibers: practical considerations and connection to mechanical properties, *J. Mater. Sci.*, 2021, **56**(27), 15087–15121, DOI: 10.1007/s10853-021-06225-1.

67 C. Muñoz-Ferreiro, C. López-Pernía, Á. Gallardo-López and R. Poyato, Unravelling the optimization of few-layer graphene crystallinity and electrical conductivity in ceramic composites by raman spectroscopy, *J. Eur. Ceram. Soc.*, 2021, **41**(16), 290–298, DOI: 10.1016/j.jeurceramsoc.2021.09.025.

68 Y.-S. Ding, *et al.*, Characteristics of graphite anode modified by CVD carbon coating, *Surf. Coat. Technol.*, 2006, **200**(9), 3041–3048, DOI: 10.1016/j.surfcoat.2005.05.040.

69 H. Qiu, *et al.*, The InnoRec Process: A Comparative Study of Three Mainstream Routes for Spent Lithium-ion Battery Recycling Based on the Same Feedstock, *Sustainability*, 2024, **16**(9), 3876, DOI: 10.3390/su16093876.

70 J. Gao, X. Bu, L. Dong, Y. Qiu, G. Xie and S. Chehreh Chelgani, Natural graphite froth flotation-an overview, *Miner. Process. Extr. Metall. Rev.*, 2025, **46**(2), 306–323, DOI: 10.1080/08827508.2024.2305384.

71 A. Vanderbruggen, *et al.*, Lithium-ion battery recycling–influence of recycling processes on component liberation

and flotation separation efficiency, *ACS ES&T Eng.*, 2022, **2**(11), 2130–2141, DOI: **10.1021/acsestengg.2c00177**.

72 A. Porvali, T. Mäkelä and J. Bachér, Observations on the leaching of milled black mass with additives, *J. Sustainable Metall.*, 2023, **9**(2), 816–825, DOI: **10.1007/s40831-023-00690-5**.

73 A. M. Salces, I. Bremerstein, M. Rudolph and A. Vanderbruggen, Joint recovery of graphite and lithium metal oxides from spent lithium-ion batteries using froth flotation and investigation on process water re-use, *Miner. Eng.*, 2022, **184**, 107670, DOI: **10.1016/j.mineng.2022.107670**.

74 X. Wang, S. Zhou, X. Bu, C. Ni, G. Xie and Y. Peng, Investigation on interaction behavior between coarse and fine particles in the coal flotation using focused beam reflectance measurement (FBRM) and particle video microscope (PVM), *Sep. Sci. Technol.*, 2021, **56**(8), 1418–1430, DOI: **10.1080/01496395.2020.1777428**.